AN APPROACH FOR ASSESSING DELAMINATION PROPAGATION CAPABILITIES IN COMMERCIAL FINITE ELEMENT CODES

Ronald Krueger

SPECIFY one ASC TECHNICAL DIVISION for this paper by highlighting one of the following:
Analysis, Design and testing
Process and Manufacturing
Durability and Damage Tolerance
Emerging Technologies
Applications
Education

Specify Name of Session/ Session Chair if invited paper of pre-arranged submission:
Special sessions to honor T. Kevin O'Brien

ABSTRACT

An approach to assessing the delamination propagation capabilities in commercial finite element codes is presented and demonstrated for one code. For this investigation, the Double Cantilever Beam (DCB) specimen and the Single Leg Bending (SLB) specimen were chosen for full three-dimensional finite element simulations. First, benchmark results were created for both specimens. Second, starting from an initially straight front, the delamination was allowed to propagate. Good agreement between the load-displacement relationship obtained from the propagation analysis results and the benchmark results could be achieved by selecting the appropriate input parameters. Selecting the appropriate input parameters, however, was not straightforward and often required an iterative procedure. Qualitatively, the delamination front computed for the DCB specimen did not take the shape of a curved front as expected. However, the analysis of the SLB specimen yielded a curved front as may be expected from the distribution of the energy release rate and the failure index across the width of the specimen. Overall, the results are encouraging but further assessment on a structural level is required.

INTRODUCTION

One of the most common failure modes for composite structures is delamination [1, 2]. The remote loadings applied to composite components are typically resolved into interlaminar tension and shear stresses at discontinuities that create mixed-mode I, II and III delaminations. To characterize the onset and growth of these delaminations, the use of fracture mechanics has become common practice over the past two decades [1, 3, 4]. The total strain energy release rate, G_T, the mode I component due to interlaminar tension, G_I, the mode II component due to interlaminar sliding shear, G_{II}, and the mode III component, G_{III}, due to interlaminar scissoring shear, as shown in Figure 1, need to be calculated. In order to predict delamination

R. Krueger, National Institute of Aerospace, 100 Exploration Way, Hampton, VA, 23666, resident at Durability, Damage Tolerance and Reliability Branch, MS 188E, NASA Langley Research Center, Hampton, VA, 23681, USA.

onset or growth for two-dimensional problems, these calculated G components are compared to interlaminar fracture toughness properties measured over a range from pure mode I loading to pure mode II loading [5-7]. A quasi static mixed-mode fracture criterion is determined by plotting the interlaminar fracture toughness, G_c, versus the mixed-mode ratio, G_{II}/G_T, determined from data generated using pure mode I Double Cantilever Beam (DCB) (G_{II}/G_T=0), pure mode II End-Notched Flexure (ENF) (G_{II}/G_T=1), and Mixed-Mode Bending (MMB) tests of varying ratios, as shown in Figure 2a for T300/914C and Figure 2b for C12K/R6376 [8, 9]. A curve fit of these data is performed to determine a mathematical relationship between G_c and G_{II}/G_T. [10, 11]. Failure is expected when, for a given mixed-mode ratio G_{II}/G_T, the calculated total energy release rate, G_T, exceeds the interlaminar fracture toughness, G_c. An interaction criterion incorporating the scissoring shear (mode III), was recently proposed by Reeder [12]. The edge-cracked torsion test (ECT) is being considered for standardization [13, 14].

The virtual crack closure technique (VCCT) is widely used for computing energy release rates based on results from continuum (2D) and solid (3D) finite element analyses and to supply the mode separation required when using the mixed-mode fracture criterion [15, 16]. An increased interest in using a fracture mechanics based approach to assess the damage tolerance of composite structures in the design phase and during certification has also renewed the interest in the virtual crack closure technique. The VCCT technique was recently implemented into the commercial finite element code ABAQUS® and MD NASTRAN™ [17, 18]. The implementation into the commercial finite element code SAMCEF® [19] is a mix of VCCT and the Virtual Crack Extension Method suggested by Parks [20]. As new approaches for analyzing composite delamination are incorporated in finite element codes, the need for comparison and benchmarking becomes important.

The objective of this study was to create an approach which allows the assessment of delamination propagation capabilities in commercial finite element codes. The approach is demonstrated for the commercial finite element code ABAQUS® with focus on their implementation of the Virtual Crack Closure Technique (VCCT) [17]. For this investigation, the Double Cantilever Beam (DCB) specimen with a unidirectional layup and the Single Leg Bending (SLB) specimen with multi-directional layup (as shown in Figure 3) were chosen for full three-dimensional finite element simulations. These specimen configurations were chosen, since a number of combined experimental and numerical studies had been performed previously where the critical strain energy release rates were evaluated [21, 23-25]. First, benchmark results were created using models simulating specimens with different delamination lengths. For each delamination length modeled, the load and displacement at the load point were monitored. The mixed-mode strain energy release rate components were calculated along the delamination front across the width of the specimen. A failure index was calculated by correlating the results with the mixed-mode failure criterion of the graphite/epoxy material. It was assumed that the delamination propagated when the failure index reached unity. Thus, critical loads and critical displacements for delamination onset were calculated for each delamination length modeled. These critical load/displacement results were used as a benchmark. Second, starting from an initially straight front, the delamination was allowed to propagate based on the algorithms implemented into VCCT for ABAQUS®. VCCT control parameters were varied to study the effect on the computed load-displacement behavior during

propagation. It was assumed that the computed load-displacement relationship should closely match the benchmark results established earlier. As a qualitative assessment, the shape of the computed delamination fronts were also compared to photographs of failed specimens.

SPECIMEN DESCRIPTION

For the current numerical investigation, the Double Cantilever Beam (DCB) and the Single Leg Bending (SLB) specimens, as shown in Figure 3, were chosen. The DCB specimen is used to determine the mode I interlaminar fracture toughness, G_{IC} (G_{II}/G_T=0) [5]. The SLB specimen was introduced for the determination of fracture toughness as a function of mixed-mode I/II ratio [21, 22]. This test may be performed in a standard three-point-bending fixture such as that used for the ENF test. By varying the relative thickness of the delaminated regions (t_1 and t_2), a different mixed-mode ratio may be achieved. This type of specimen was chosen to study mode separation. Previously, a number of combined experimental and numerical studies of these specimens had been performed where the critical strain energy release rates were evaluated [21, 23-25].

In general, mode I, mode II and mixed-mode tests are performed on unidirectionally reinforced laminates, which means that delamination growth occurs at a [0/0] interface and crack propagation is parallel to the fibers. For the current study, a DCB specimen made of T300/1076 graphite/epoxy with a unidirectional layup, $[0]_{24}$, was modeled. Although this unidirectional layup is desired for standard test methods to characterize fracture toughness, delamination growth between layers of the same orientation will rarely occur in real structures. Previously, combined experimental and numerical studies on specimens with multidirectional layups were performed where the critical strain energy release rates of various interfaces were evaluated under mode I, mode II and mixed-mode conditions [21, 24]. Therefore, a SLB-specimen made of C12K/R6376 graphite/epoxy with a multidirectional layup was selected. The stacking sequence $[\pm30/0/-30/0/30/0_4/30/0/-30/0/-30/30/_\uparrow-30/30/0/30/0/-30/0_4/30/0/30/0/\pm30]$ was designated D$\pm$30, where the arrow denotes the location of the delamination. The material properties are given in Table I.

METHODOLOGY
Fracture Criteria

Linear elastic fracture mechanics has proven useful for characterizing the onset and growth of delaminations in composite laminates [3, 4]. A quasi static mixed-mode fracture criterion is determined by plotting the interlaminar fracture toughness, G_c, versus the mixed-mode ratio, G_{II}/G_T. Typical examples are presented in Figure 2 for T300/914C and C12K/R6376 carbon epoxy materials. A fracture criterion was suggested by Benzeggah and Kenane [11] using a simple mathematical relationship between G_c and G_{II}/G_T

$$G_c = G_{Ic} + \left(G_{IIc} - G_{Ic}\right) \cdot \left(\frac{G_{II}}{G_T}\right)^{\eta}. \tag{1}$$

In this expression, G_{Ic} and G_{IIc} are the experimentally-determined fracture toughness data for mode I and II as shown in Figure 2. The factor η was determined by a curve fit using the Levenberg-Marquardt algorithm in KaleidaGraph[TM] graphing and data analysis software [26]. Fracture initiation is expected when, for a given mixed-mode ratio G_{II}/G_T, the calculated total energy release rate, G_T, exceeds the interlaminar fracture toughness, G_c and therefore the failure index G_T/G_c is equal or greater than unity

$$\frac{G_T}{G_c} \geq 1. \tag{2}$$

For three-dimensional analysis, which yields results for the scissoring mode G_{III}, a modified definition is introduced where G_S denotes the sum of the in-plane shearing components $G_{II}+G_{III}$ [27]. This modification becomes necessary if a mixed-mode failure criterion, which accounts for all three modes, is not available. For analyses where $G_{III}=0$, this definition is equal to the commonly used definition of the mixed-mode ratio, G_{II}/G_T mentioned above. To determine failure along the delamination front, the critical energy release rate G_c is calculated using equation (1) with $G_{II} = G_S$ at each point along the delamination front. Subsequently, the failure index G_T/G_c is determined as above. The modified interaction criterion is an integral part of the VCCT for ABAQUS[®] analysis software and may be selected by the user [17].

Recently, Reeder [12] suggested an interaction criterion that is based on the fracture criterion suggested by Benzeggah and Kenane but incorporates the mode III shear [12]

$$G_c = G_{Ic} + \left(G_{IIc} - G_{Ic}\right) \cdot \left(\frac{G_{II} + G_{III}}{G_T}\right)^{\eta} + \left(G_{IIIc} - G_{IIc}\right) \cdot \frac{G_{III}}{G_{II} + G_{III}} \cdot \left(\frac{G_{II} + G_{III}}{G_T}\right)^{\eta} \tag{3}$$

which is also an integral part of the VCCT for ABAQUS[®] analysis software and may be selected by the user [17].

Virtual Crack Closure Technique (VCCT)

A variety of methods are used in the literature to compute the strain energy release rate based on results obtained from finite element analysis. For delaminations in laminated composite materials where the failure is highly dependent on the mixed-mode ratio (as shown in Figure 2), the virtual crack closure technique (VCCT) [15, 16] has been most widely used for computing energy release rates. VCCT calculations using continuum (2D) and solid (3D) finite element analyses provide the mode separation required when using the mixed-mode fracture criterion.

Currently, VCCT for ABAQUS[®] is an add-on capability to ABAQUS[®]/Standard Versions 6.5, 6.6 and 6.7 that provides a specific implementation of the virtual crack

closure technique within ABAQUS®. The plane of delamination in three-dimensional analyses is modeled using the existing ABAQUS®/Standard crack propagation capability based on the contact pair capability [17]. Beyond simple calculations of the mixed-mode strain energy release rates along the delamination front – which was studied previously [25] - the implementation also offers a crack propagation capability in ABAQUS®. Once the energy release rate exceeds the critical strain energy release rate (including the user-specified mixed-mode criteria as shown in Figure 2), the node at the crack tip is released in the following increment, which allows the crack to advance [17].

In addition to the mixed-mode fracture criterion, VCCT for ABAQUS® requires, additional input for the propagation analysis. If a user specified release tolerance is exceeded in an increment $(G - G_c)/G_c > \text{release tolerance}$, a cutback operation is performed which reduces the time increment. In the new smaller increment, the strain energy release rates are recalculated and compared to the user specified cutback tolerance. The cutback reduces the degree of overshoot and improves the accuracy of the local solution [17]. A release tolerance of 0.2 is suggested in the handbook [17].

To help overcome convergence issues during the propagation analysis, ABAQUS® provides:

- *contact stabilization* which is applied across only selected contact pairs and used to control the motion of two contact pairs while they approach each other in multi-body contact. The damping is applied when bonded contact pairs debond and move away from each other
- *automatic or static stabilization* which is applied to the motion of the entire model and is commonly used in models that exhibit statically unstable behavior such as buckling
- *viscous regularization* which is applied only to nodes on contact pairs that have just debonded. The viscous regularization causes the tangent stiffness matrix of the softening material to be positive for sufficiently small time increments.

Setting the value of the input parameters correctly is often an iterative procedure, which will be discussed later.

FINITE ELEMENT MODELING

Typical three-dimensional finite element models of Double Cantilever Beam (DCB) and Single Leg Bending (SLB) specimens are shown in Figures 4 and 5. The specimens were modeled with solid brick elements C3D8I which had yielded excellent results in a previous study [25]. Along the length, all models were divided into different sections with different mesh refinement. A refined mesh of length 5 mm with 20 elements as used for the DCB specimen is shown in the detail of Figure 4a. This section length had been selected in previous studies [23, 25] and was also used during the current investigation. Across the width, the model was divided into a center section and a refined edge section, *i*, to capture local edge effects and steep gradients. These sections appear as dark areas in the full view of the specimen as shown in Figure 4a. The DCB specimen was modeled with six elements through the specimen thickness (*2h*) as shown in the detail of Figure 4a. This model was used to calculate

mode I energy release rates and create the benchmark results discussed later. For propagation analyses using VCCT for ABAQUS®, the model with a uniform mesh across the width, as shown in Figure 4b, was used to avoid potential problems at the transition between the coarse and very fine mesh near the edges of the specimen.

The plane of delamination was modeled as a discrete discontinuity in the center of the specimen. For the analysis with VCCT for ABAQUS®, the models were created as separate meshes for the upper and lower part of the specimens with identical nodal point coordinates in the plane of delamination [17]. Two surfaces (top and bottom surface) were created on the meshes as shown in Figure 4. Additionally, a node set was created to identify the intact (bonded nodes) region.

For the SLB specimen, a model with a uniform mesh across the width was used as shown in Figure 5. For modeling convenience, the upper and lower arm were modeled similar to the model of the DCB specimen. To model the test correctly only the upper arm was supported in the analysis as shown in Figure 5. Two plies on each side of the delamination were modeled individually using one element for each ply as shown in the detail of Figure 5. Since the delamination occurs at an interface between materials with dissimilar properties, care must be exercised in interpreting the values for G_I and G_{II} obtained using the virtual crack closure technique. For interfacial delaminations between two differing orthotropic solids, the observed oscillatory singularity at the crack tip becomes an issue for small element lengths [28, 29]. Hence, a value of crack tip element length, Δa, was chosen (approximately three ply thicknesses) in the range over which the strain energy release rate components exhibit a reduced sensitivity to the value of Δa. The adjacent four plies were modeled by one element with material properties smeared using the rule of mixtures [30, 31]. This procedure did not calculate the full A-B-D stiffness matrix contributions of the plies, however, it appeared suitable to enforce a reasonable model size. The adjacent element extended over the four 0° plies. The six outermost plies were modeled by one element with smeared material properties.

ANALYSIS

First, models simulating specimens with different delamination lengths were analyzed. For each delamination length modeled, the load and displacement at the load point were monitored. The mixed-mode strain energy release rate components were calculated along the delamination front across the width of the specimen. A failure index was calculated by correlating the results with the mixed-mode failure criterion of the graphite/epoxy material. It was assumed that the delamination propagated when the failure index reached a value of unity. Thus, critical loads and critical displacements for delamination onset were calculated for each delamination length modeled. These critical load/displacement results were used as a benchmark. Second, starting from an initially straight front, the delamination was allowed to propagate based on the algorithm implemented into VCCT for ABAQUS®. Input parameters were varied to study the effect on the computed load-displacement behavior during propagation. It was assumed that the computed load-displacement relationship should closely match the benchmark results established earlier. As a qualitative assessment, the shape of the computed delamination fronts were also compared to photographs of failed specimens.

Creating a Benchmark Solution for DCB specimens

The computed mode I strain energy release rate values were plotted versus the normalized width, *y/B*, of the specimen as shown in Figure 6a. The results were obtained from models shown in Figure 4a for seven different delamination lengths *a*. An opening displacement $\delta/2$=1.0 mm was applied to each arm of the model. Qualitatively, the mode I strain energy release rate is fairly constant in the center part of the specimen and drops progressively towards the edges. This distribution will cause the initial straight front to grow into a curved front as explained in detail in the literature [32, 33]. As expected, the mode II and mode III strain energy release rates were computed to be nearly zero and hence are not shown. Computed mode I strain energy release rates decreased with increasing delamination length *a*.

The failure index G_T/G_c was computed based on a mode I fracture toughness G_{Ic}=170.3 J/m^2 for T300/914C (see Figure 2). The failure index was plotted versus the normalized width, *y/B*, of the specimen as shown in Figure 6b. For all delamination lengths modeled – except for *a*=40 mm - the failure index in the center of the specimen (*y/B*=0) is above unity ($G_T/G_c \geq 1$).

For all delamination lengths modeled, the reaction loads *P* at the location of the applied displacement were calculated and plotted versus the applied opening displacement $\delta/2$ as shown in Figure 7a. The critical load, P_{crit}, when the failure index in the center of the specimen (*y/B*=0) reaches unity (G_T/G_c=1), can be calculated based on the relationship between load *P* and the energy release rate *G* [34].

$$G = \frac{P^2}{2} \cdot \frac{\partial C_P}{\partial A} \tag{4}$$

In equation (4), C_P is the compliance of the specimen and ∂A is the increase in surface area corresponding to an incremental increase in load or displacement at fracture. The critical load P_{crit} and critical displacement $\delta_{crit}/2$ were calculated for each delamination length modeled

$$\frac{G_T}{G_c} = \frac{P^2}{P_{crit}^2} \quad \Rightarrow \quad P_{crit} = P\sqrt{\frac{G_c}{G_T}} \ , \quad \delta_{crit} = \delta\sqrt{\frac{G_c}{G_T}} \tag{5}$$

and the results were included in the load/displacement plots as shown in Figure 7a. The results indicate that, with increasing delamination length, less load is required to extend the delamination. This means that the DCB specimen exhibits unstable delamination growth under load control. Therefore, prescribed opening displacements $\delta/2$ were applied in the analysis instead of nodal point loads P to avoid problems with numerical stability of the analysis. It was assumed that the critical load/displacement results can be used as a benchmark. For the delamination propagation, therefore, the load/displacement results obtained from the model of a DCB specimen with an initially straight delamination of *a*=30 mm length should correspond to the critical load/displacement path (in red) in Figure 7a.

Delamination Propagation in a DCB Specimen using VCCT for ABAQUS®

The propagation analysis was performed in two steps using the model shown in Figure 4b for a delamination length 30 mm. In the first step, a prescribed displacement ($\delta/2= 0.74$ mm) was applied in two increments which equaled nearly the critical tip opening ($\delta_{crit}/2= 0.75$ mm) determined in the analysis above for a delamination length of a=30 mm. In the second step, the total prescribed displacement was increased ($\delta/2= 2.8$ mm). Automatic incrementation was used with a small increment size at the beginning (10^{-4} of the total increment) and a very small minimum allowed increment (10^{-18} of the total increment) to reduce the risk of numerical instability and early termination of the analysis. The analysis was limited to 1000 increments. Initially, analyses were performed without stabilization or viscous regularization. Release tolerance values between 0.2 and 0.6 were used. Using the parameters, the analysis terminated early prior to advancing the delamination.

In Figures 7b and 8(a-b), the computed resultant force (load P) at the tip of the DCB specimen is plotted versus the applied crack tip opening ($\delta/2$) for different input parameters which are listed in Table II. For the results shown, the analysis terminated when the 1000 increment limit set for the analysis was reached. Several analyses terminated early because of convergence problems. To overcome the convergence problems, the methods implemented in ABAQUS® were used individually to study the effects. For the results plotted in Figure 7b, global stabilization was added to the analysis. For a stabilization factor of 2×10^{-5}, the stiffness changed to almost infinity once the critical load was reached causing the load to increase sharply (plotted in blue). The load increased until a point was reached where the delamination propagation started and the load gradually decreased following a zigzag curve with local rising and declining segments. The gradual load decrease followed the same trend as the benchmark curve (in grey) but is shifted toward higher loads. For a stabilization factor of 2×10^{-6} (in green), the same zigzag pattern was observed but the average curve was in good agreement with the benchmark result. For a stabilization factor of 2×10^{-7} (in red), the average was lower than before but was in good agreement with the benchmark result until termination after 550 increments due to convergence problems. The results obtained for a stabilization factor of 2×10^{-8} (in black for a release tolerance of 0.2) were on top of the previous result. The rate of convergence appeared to be slower since only $\delta/2= 1.14$ mm was applied for 1000 increments compared to $\delta/2= 1.24$ mm for a stabilization factor of 2×10^{-6} and the same release tolerance (0.2). Changing the release tolerance also appeared to influence the convergence as shown in Table II. For a release tolerance of 0.02, the analysis terminated after 1000 increments for $\delta/2= 1.04$ mm. For a release tolerance of 0.002, the analysis terminated due to convergence problems after 451 increments. Changing the release tolerance, however, appeared to have no effect on the overall load/displacement behavior or the magnitude of the zigzag pattern.

For the results plotted in Figure 8a, contact stabilization was added to the analysis. For all combinations of stabilization factors and release tolerances, a zigzag pattern was observed, where the peak values were in good agreement with the benchmark result. The zigzag curve is slightly lower. Decreasing the stabilization factors appeared to cause a slower rate of convergence which is either seen by smaller $\delta/2$ for the same number of analysis increments or early termination of the analysis as shown

in Table II. Changing the release tolerance also appeared to influence the convergence. However, it appeared to have no effect on the overall load/displacement behavior or the magnitude of the zigzag pattern.

Viscous regularization was added to the analysis to overcome convergence problems. Convergence could not be achieved over a wide range of viscosity coefficients when a release tolerance value of 0.2 was used as suggested in reference [17]. Subsequently, the release tolerance value was increased. The results where convergence was achieved are plotted in Figure 8b. For all combinations of the viscosity coefficient and release tolerance, a zigzag pattern was obtained, where the peak values were in good agreement with the benchmark result. The average results are somewhat lower than the benchmark result. Compared to results obtained from analyses with global and contact stabilization, the results obtained with viscous regularization appear to have a better rate of convergence since a higher opening displacement ($\delta/2$= 1.48 mm) was applied during the analysis for the same number of total increments (1000). Decreasing the viscosity coefficient appeared to cause a slower rate of convergence which was seen by smaller $\delta/2$ values for the same number of analysis increments as visible in the plots. Lowering the release tolerance also appeared to influence the convergence which was either seen by smaller $\delta/2$ for the same number of analysis increments as visible in the plots or early termination of the analysis as shown in Table II. Changing the release tolerance, however, appeared to have no effect on the overall load/displacement behavior or the magnitude of the zigzag pattern.

In summary, good agreement between analysis results and the benchmark could be achieved for different release tolerance values in combination with global or contact stabilization or viscous regularization. Selecting the appropriate input parameters, however, was not straightforward and often required several iterations where the parameters had to be changed. All results had a zigzag pattern.

Besides matching the load displacement behavior of benchmark results, a delamination propagation analysis should also yield a delamination front shape that is representative of the actual failure. An example of delamination front shapes observed by opening a tested DCB specimen are shown in Figure 9a [35]. From the initial straight delamination front which is formed by the edge of the Teflon insert, the delamination develops into a curved thumb nail shaped front. The front remains thumbnail shaped if the test is continued and the delamination continues to grow. Delamination propagation computed using the model with a uniform mesh across the width (Figure 4b) is shown in Figure 9b at the end of the analysis after 1000 increments. Plotted on the bottom surface (defined in Figure 4b) are the contours of the bond state, where the delaminated section appears in red and the intact (bonded) section in blue. The transition between the colors indicates the location of the delamination front. The initial straight front was included for clarification. The first propagation was observed in the center of the specimen as expected from the distribution of the energy release rate (Figure 6a) and the failure index (Figure 6b). The front propagated across the width of the specimen until a new straight front was reached. Subsequently, the propagation starts again in the center. During the analysis, the front never developed into the expected curved thumbnail front, and the analysis terminated with a straight front as shown in Figure 9b. This result is somewhat unsatisfactory but may be explained by the fact that the failure index in this particular example is nearly constant across about 80% of the width of the specimen as shown in

Figure 6b. An even finer mesh may be required to capture the lagging propagation near the edge.

Creating a Benchmark Solution for SLB specimens

The computed total strain energy release rate values were plotted versus the normalized width, y/B, of the SLB specimen as shown in Figure 10a. The results were obtained from models shown in Figure 5 for twelve different delamination lengths a. An arbitrary center deflection w=2.8 mm was applied as shown in Figure 5. Qualitatively, the total energy release rate is fairly constant in the center part of the specimen and drops towards the edges. Peaks in the distribution are observed at the edges. Computed total strain energy release rates decreased with increasing delamination length a. The sum of the shear components $G_S = G_{II}+G_{III}$ and the mixed-mode ratio G_S/G_T were also calculated for each nodal point along the delamination front across the width of the specimen (not shown).

Using the mixed-mode failure criterion for C12K/R6376 (see Figure 2b), the failure index G_T/G_c was computed for each node along the delamination front and plotted versus the normalized width, y/B, of the specimen as shown in Figure 10b. For the center deflection applied, the failure index G_T/G_c in the center is well below one. The failure index is almost constant in the center of the specimen, drops towards the edges and increases again in the immediate vicinity of the edge. To reach G_T/G_c=1 in the center of the specimen (y/B=0), a critical center deflection, w_{crit}, and corresponding critical load P_{crit}, were calculated using equation (5) for all delamination lengths modeled.

For all delamination lengths modeled, the reaction load P at the location of the applied deflection were calculated and plotted versus the applied center deflection, w, as shown in Figure 11a. The calculated critical center deflection, w_{crit}, and corresponding critical load values, P_{crit}, were included in the plots. The results indicated that, with increasing delamination length, less load is required to extend the delamination. At the same time also, the values of the critical center deflection decreased. This means that the SLB specimen exhibits unstable delamination growth under load as well as displacement control. From these critical load/displacement results, a benchmark solution can be created. To define the benchmark, it is assumed that prescribed center deflections are applied in the analysis instead of nodal point loads P to minimize problems with numerical stability of the analysis caused by the unstable growth. Once the critical center deflection is reached and delamination propagation starts, the applied displacement must be held constant over several increments while the delamination front is advanced during these increments. Once the stable path is reached, the applied center deflection is increased again incrementally. For the simulated delamination propagation, therefore, the load/displacement results obtained from the model of a SLB specimen with an initially straight delamination length of a=34 mm should correspond to the critical load/displacement path (in red) as shown in Figure 11a.

Delamination Propagation in a SLB Specimen using VCCT for ABAQUS®

The propagation analysis was performed in two steps using the model shown in Figure 5. In the first step, a central deflection (w= 3.1 mm) was applied in two increments which equaled nearly the critical tip opening (w_{crit}= 3.23 mm) determined in the analysis above. In the second step, the total prescribed displacement was increased (w= 5.0 mm). Automatic time incrementation was used with a small initial time increment size (10^{-3}) and a very small minimum allowed time increment (10^{-17}) to reduce the risk of numerical instability and early termination of the analysis. The analysis was limited to 1000 increments.

In Figure 11b and 12(a-b), the computed resultant force (load P) at the center of the SLB specimen is plotted versus the center deflection (w) for different input parameters which are listed in Table II. The analysis terminated before the total prescribed center deflection was applied. For the results shown, the analysis terminated when the 1000 increment limit set for the analysis was reached. Several analyses terminated early because of convergence problems. The results computed when global stabilization was used are plotted in Figure 11b. For a stabilization factor of 2×10^{-5}, the load increased suddenly at the beginning of the second load step (plotted in blue). Then, the load continued to increase on a path with the same stiffness as the benchmark but offset to higher loads. The load continued to increase until a point was reached where delamination propagation started and the load decreased. The analysis was stopped by the user. For a stabilization factor of 2×10^{-6} (in green), the delamination growth started at the critical center deflection. In the beginning, the load/displacement path followed the constant deflection branch of the benchmark result very well. At the transition between the constant deflection branch and the stable propagation branch of the benchmark result, the applied center deflection was about 2% higher compared to the benchmark. For the stable path, a zigzag pattern was observed but the minimum is in good agreement with the benchmark result.

The results computed when contact stabilization was used are plotted in Figure 12a. For a small stabilization factor (1×10^{-6}) and a release tolerance (0.2) suggested in the handbook [17], the load dropped and delamination propagation started prior to reaching the critical point of the benchmark solution (plotted in blue). The load/displacement path then ran parallel to the constant deflection branch of the benchmark result but the analysis terminated early due to convergence problems. The stabilization factor and release tolerance had to be increased to avoid premature termination of the analysis. For a stabilization factor of 1×10^{-5} and release tolerance of 0.5 (in green), the load dropped at the critical point of the benchmark solution. First, the center deflection kept increasing with decreasing load. Later, the load/displacement path ran parallel to the constant deflection branch of the benchmark result. At the transition between the constant deflection branch and the stable propagation branch of the benchmark result, the applied center deflection was about 2% higher compared to the benchmark. For the stable path, a zigzag pattern was observed where the average results were in good agreement with the benchmark result. The difference between the maximum and minimum values was much smaller than in the case where global stabilization was used. The best results compared to the benchmark were obtained for even higher values of the stabilization factors of 1×10^{-4} and a release tolerance of 0.5 (in red).

When viscous regularization was used to help overcome convergence issues, a value of 0.2 was used initially for the release tolerance as suggested in the handbook [17]. Convergence could not be achieved which led to an increase in release tolerance. The results are plotted in Figure 12b. For a small viscosity coefficient of $1x10^{-4}$ and a release tolerance of 0.5 (in blue), the load dropped at the critical point, but the center deflection kept increasing with decreasing load. Then, the analysis terminated early due to convergence problems. For an increased viscosity coefficient of $1x10^{-2}$ and a release tolerance of 0.5 (in red), the load dropped at the critical point and the load/displacement path started following the constant deflection branch of the benchmark result, but the analysis terminated early due to convergence problems. The viscosity coefficient and release tolerance had to be increased further to avoid premature termination of the analysis. For a viscosity coefficient of $1x10^{-1}$ and a release tolerance of 0.9 (in green), the load dropped at the critical point. First, the center deflection kept increasing with decreasing load. Later, the load/displacement path ran parallel to the constant deflection branch of the benchmark result. At the transition between the constant deflection branch and the stable propagation branch of the benchmark result, the applied center deflection is about 2.5% higher compared to the benchmark. For the stable path, a zigzag pattern is observed where the average results are in good agreement with the benchmark result. The difference between the maximum and minimum values is much smaller compared to the cases where global or contact stabilization was used.

In summary, good agreement between analysis results and the benchmark could be achieved for different release tolerance values in combination with global or contact stabilization or viscous regularization. Selecting the appropriate input parameters, however, was not straightforward and often required several iterations where the parameters had to be changed.

Delamination propagation computed using the model with a uniform mesh across the width (Figure 5) is shown in Figure 13 after 1000 increments. Plotted on the bottom surface (defined in Figure 5) are the contours of the bond state variable. The bond state varies between 0.0 (fully bonded shown in dark blue) and 1.0 (fully disbonded shown in red) [17]. The transition between the colors indicated the location of the delamination front. The initial straight front was included for clarification. The first propagation is observed near the center and corresponds to the maximum in the distribution of the failure index (Figure 10b). The front then propagated across the width. Further propagation created a curved front where the edges lag behind as shown in Figure 13. This result is in good agreement with expectations based on the distribution of the failure index shown in Figure 10b. C-scans or x-ray photographs of tested specimens were not available for comparison.

SUMMARY AND CONCLUSIONS

An approach for assessing the delamination propagation capabilities in commercial finite element codes is presented and demonstrated for the commercial finite element code ABAQUS® with focus on their implementation of the Virtual Crack Closure Technique (VCCT). For this investigation, the Double Cantilever Beam (DCB) specimen with a unidirectional layup and the Single Leg Bending (SLB) specimen with a multi-directional layup were chosen for full three-dimensional finite

element simulations. First, critical load/displacement results were defined for delamination onset which were used subsequently as benchmarks. Second, starting from an initially straight front, the delamination was allowed to propagate based on the algorithms implemented into VCCT for ABAQUS®. VCCT control parameters were varied to study the effect on the computed load-displacement behavior during propagation. It was assumed that for good results the computed load-displacement relationship should correspond to the benchmark results established earlier. Third - as a qualitative assessment - the shape of the computed delamination fronts were also compared to photographs of failed specimens.

Good agreement between the load-displacement relationship obtained from the propagation analysis results and the benchmark results could be achieved by selecting the appropriate input parameters, however, a zigzag response was obtained during propagation. Selecting the appropriate VCCT input parameters such as release tolerance, global or contact stabilization and viscous regularization, however, was not straightforward and often required an iterative procedure. In this case, the input parameters were modified until the analysis results agreed with the benchmark. For all the combinations of input parameters, only a global stabilization factor of 2×10^{-6} in combination with a release tolerance of 0.2 gave good results for the DCB and SLB simulations. In a real case scenario where the results are unknown, obtaining the right solution will remain challenging.

Besides matching the load displacement behavior of the benchmark results, a delamination propagation analysis should also yield a delamination front shape that is representative of the actual failure. During the analysis of the DCB specimen, the front never developed into the expected curved thumbnail front as seen in tested specimens. The analysis terminated with a straight front which is somewhat unsatisfactory. The result may be explained by the fact that the failure index in this particular example is constant across about 80% of the width of the specimen and a finer mesh may be required to capture the lagging propagation near the edge. During the analysis of the SLB specimen, the front developed into a curved front as expected from the distribution of the failure index. This result is encouraging. Overall, the results are promising but further studies are required which should include different levels of mesh refinement, new stabilization options and the use of continuum shell elements to model the specimens. Additionally, assessment of the propagation capabilities in more complex specimens and on a structural level is required.

ACKNOWLEDGEMENTS

REFERENCES

[1] T.K. O'Brien, *Characterization of Delamination Onset and Growth in a Composite Laminate*, in Damage in Composite Materials, ASTM STP 775,: American Society for Testing and Materials, pp. 140-167, 1982.

[2] T.E. Tay, *Characterization and Analysis of Delamination Fracture in Composites - An Overview of Developments from 1990 to 2001*, Applied Mechanics Reviews, vol. 56, pp. 1-32, 2003.

[3] R.H. Martin, *Incorporating Interlaminar Fracture Mechanics Into Design*, in International Conference on Designing Cost-Effective Composites: IMechE Conference Transactions, London, U.K., pp. 83-92, 1998.

[4] T.K. O'Brien, *Fracture Mechanics of Composite Delamination*, in ASM Handbook, Volume 21, Composites: ASM International, pp. 241-245, 2001.

[5] *ASTM D 5528-94a, Standard Test Method for Mode I Interlaminar Fracture Toughness of Unidirectional Fiber-Reinforced Polymer Matrix Composites*, in Annual Book of ASTM Standards, vol. 15.03: American Society for Testing and Materials, 2000.

[6] *ASTM D 6671-01, Standard Test Method for Mixed Mode I-Mode II Interlaminar Fracture Toughness of Unidirectional Fiber Reinforced Polymer Matrix Composites*, in Annual Book of ASTM Standards, vol. 15.03: American Society for Testing and Materials, 2000.

[7] R.H. Martin and B.D. Davidson, *Mode II Fracture Toughness Evaluation Using A Four Point Bend End Notched Flexure Test*, Plastics, Rubber and Composites, vol. 28, pp. 401-406, 1999.

[8] M. König, R. Krüger, K. Kussmaul, M. v. Alberti, and M. Gädke, *Characterizing Static and Fatigue Interlaminar Fracture Behaviour of a First Generation Graphite/Epoxy Composite*, in Composite Materials: Testing and Design - (13th Vol.), ASTM STP 1242, S.J. Hooper, Ed.: American Society for Testing and Materials, pp. 60-81, 1997.

[9] B.D. Davidson and W. Zhao, *An Accurate Mixed-Mode Delamination Failure Criterion for Laminated Fibrous Composites Requiring Limited Experimental Input,* submitted to, Composites Science and Technology, 2006.

[10] T.K. O'Brien, *Composite Interlaminar Shear Fracture Toughness, G_{IIc}: Shear Measurement or Sheer Myth ?*, in Composite Materials: Fatigue and Fracture, Seventh Volume, ASTM STP 1330, pp. 3-18, 1998.

[11] M.L. Benzeggagh and M. Kenane, *Measurement of Mixed-Mode Delamination Fracture Toughness of Unidirectional Glass/Epoxy Composites with Mixed-Mode Bending Apparatus*, Composites Science and Technology, vol. 56, pp. 439-449, 1996.

[12] J. Reeder, *3D Mixed-Mode Delamination Fracture Criteria - An Experimentalist's Perspective*, presented at American Society for Composites, 21st Annual Technical Conference, Dearborn, Michigan, 2006.

[13] S.M. Lee, *An Edge Crack Torsion Method for Mode III Delamination Fracture Testing*, J. of Composite Technology and Research., pp. 193-201, 1993.

[14] J.G. Ratcliffe, *Characterization of the Edge Crack Torsion (ECT) Test for Mode III Fracture Toughness Measurement of Laminated Composites*, NASA/TM-2004-213269 , 2004.

[15] E.F. Rybicki and M.F. Kanninen, *A Finite Element Calculation of Stress Intensity Factors by a Modified Crack Closure Integral*, Eng. Fracture Mech., vol. 9, pp. 931-938, 1977.

[16] R. Krueger, *Virtual Crack Closure Technique: History, Approach and Applications*, Applied Mechanics Reviews, vol. 57, pp. 109-143, 2004.

[17] *VCCT for ABAQUS - User's Manual*, ABAQUS 2005.

[18] *MSC NASTRAN: Industry-Leading Linear and Nonlinear Finite Element Analysis Solver.* MSC Software Data Sheet, 2007.

[19] M. Bruyneel, P. Morelle, and J.-P. Delsemme, *Failure Analysis of Metallic and Composite Structures with SAMCEF*, in NAFEMS Seminar: Materials Modeling – FE Simulations of the Behavior of Modern Industrial Materials Including their Failure. Niedernhausen, Germany, 2006.

[20] D.M. Parks, *The Virtual Crack Extension Method for Nonlinear Material Behavior*, Computer Methods in Applied Mechanics and Engineering, vol. 12, pp. 353-364, 1977.

[21] B.D. Davidson, R. Krüger, and M. König, *Three Dimensional Analysis of Center Delaminated Unidirectional and Multidirectional Single Leg Bending Specimens*, Composites Science and Technology, vol. 54, pp. 385-394, 1995.

[22]   A. Pieracci, B.D. Davidson, and V. Sundararaman, *Nonlinear Analyses of Homogeneous, Symmetrically Delaminated Single Leg Bending Specimens*, Journal Composite Tech. Res., vol. 20, pp. 170-178, 1998.

[23]   R. Krüger, *Three Dimensional Finite Element Analysis of Multidirectional Composite DCB, SLB and ENF Specimens*, Institute for Statics and Dynamics of Aerospace Structures, University of Stuttgart ISD-Report No. 94/2, 1994.

[24]   B.D. Davidson, R. Krüger, and M. König, *Effect of Stacking Sequence on Energy Release Rate Distributions in Multidirectional DCB and ENF specimens*, Eng. Fracture Mech., vol. 55, pp. 557-569, 1996.

[25]   R. Krueger and D. Goetze, *Influence of Finite Element Software on Energy Release Rates Computed Using the Virtual Crack Closure Technique*, NIA Report No. 2006-06, NASA/CR-214523, 2006.

[26]   *KaleidaGraph: Data Analysis/Graphing Application for Macintosh and Windows Operating Systems*: Synergy Software, 1996.

[27]   M. König, R. Krüger, and S. Rinderknecht, *Finite Element Analysis of Delamination Growth in a Multidirectional Composite ENF Specimen*, in Composite Materials: Theory and Practice, ASTM STP 1383, P. Grant and C.Q. Rousseau, Eds.: American Society for Testing and Materials, pp. 345-365, 2000.

[28]   I.S. Raju, J.H. Crews, and M.A. Aminpour, *Convergence of Strain Energy Release Rate Components for Edge-Delaminated Composite Laminates*, Eng. Fracture Mech., vol. 30, pp. 383--396, 1988.

[29]   C.T. Sun and M.G. Manoharan, *Strain Energy Release Rates of an Interfacial Crack Between Two Orthotropic Solids*, J. Composite Materials, vol. 23, pp. 460--478, 1989.

[30]   S.W. Tsai, *Theory of Composite Design*: Think Composites, 1992.

[31]   S.W. Tsai and H.T. Hahn, *Introduction to Composite Materials*: Technomic Publishing Co., Inc., 1980.

[32]   I.S. Raju, K.N. Shivakumar, and J.H. Crews, *Three-Dimensional Elastic Analysis of a Composite Double Cantilever Beam Specimen*, AIAA J., vol. 26, pp. 1493-1498, 1988.

[33]   B.D. Davidson, *An Analytical Investigation of Delamination Front Curvature in Double Cantilever Beam Specimens*, J. Composite Mat., vol. 24, pp. 1124-1137, 1990.

[34]   D. Broek, *The Practical Use of Fracture Mechanics*: Kluwer Academic Publishers, 1991.

[35]   U. Koser, *Experimentelle Ermittlung der Energiefreisetzungsrate an Matrix-Rissen im Faserverbundwerkstoff T300/976*, Diplomarbeit: Staatliche Materialprüfungsanstalt (MPA), University of Stuttgart, 1989.

TABLE 1. MATERIAL PROPERTIES.

T300/1076 Unidirectional Graphite/Epoxy Prepreg		
E_{11} = 139.4 GPa	E_{22} = 10.16 GPa	E_{33} = 10.16 GPa
v_{12} = 0.30	v_{13} = 0.30	v_{23} = 0.436
G_{12} = 4.6 GPa	G_{13} = 4.6 GPa	G_{23} = 3.54 GPa
C12K/R6376 Unidirectional Graphite/Epoxy Prepreg		
E_{11} = 146.9 GPa	E_{22} = 10.6 GPa	E_{33} = 10.6 GPa
v_{12} = 0.33	v_{13} = 0.33	v_{23} = 0.33
G_{12} = 5.45 GPa	G_{13} = 5.45 GPa	G_{23} = 3.99 GPa

The material properties are given with reference to the ply coordinate axes where index 11 denotes the ply principal axis that coincides with the direction of maximum in-plane Young's modulus (fiber direction). Index 22 denotes the direction transverse to the fiber in the plane of the lamina and index 33 the direction perpendicular to the plane of the lamina.

TABLE II. INPUT PARAMETERS.

FE model	global stabilization	contact stabilization	viscous regularization	release tolerance	last increment
DCB-st3	$2\ 10^{-5}$			0.2	381
DCB-st4	$2\ 10^{-6}$			0.2	1002
DCB-st5	$2\ 10^{-7}$			0.2	550
DCB-st6	$2\ 10^{-8}$			0.2	1002
DCB-st7	$2\ 10^{-8}$			0.02	1002
DCB-st8	$2\ 10^{-8}$			0.002	451
DCB-ct1		$1\ 10^{-5}$		0.2	1002
DCB-ct2		$1\ 10^{-6}$		0.2	1002
DCB-ct3		$1\ 10^{-7}$		0.2	751
DCB-ct4		$1\ 10^{-7}$		0.02	1002
DCB-ct5		$1\ 10^{-7}$		0.002	1002
DCB-ct6		$1\ 10^{-3}$		0.002	911
DCB-vr1			$1\ 10^{-4}$	0.5	1002
DCB-vr2			$1\ 10^{-4}$	0.3	273
DCB-vr3			$1\ 10^{-5}$	0.5	1002
DCB-vr4			$1\ 10^{-5}$	0.3	1002
SLB-st1	$2\ 10^{-5}$			0.2	266
SLB-st2	$2\ 10^{-6}$			0.2	1002
SLB-ct1		$1\ 10^{-6}$		0.2	133
SLB-ct6		$1\ 10^{-5}$		0.5	811
SLB-ct8		$1\ 10^{-4}$		0.5	1002
SLB-vr1			$1\ 10^{-4}$	0.5	65
SLB-vr6			$1\ 10^{-2}$	0.5	88
SLB-vr12			$1\ 10^{-1}$	0.9	537

P
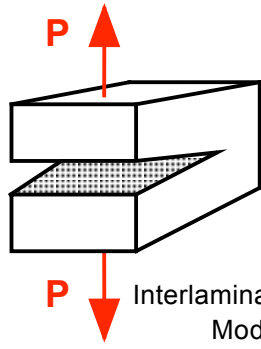
P Interlaminar tension
Mode I
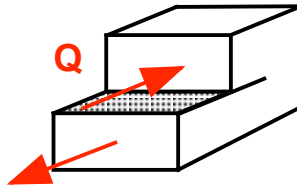
Q Interlaminar sliding shear
Mode II
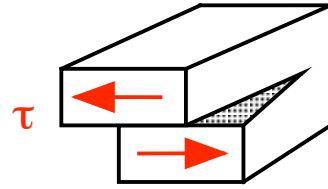
τ Interlaminar scissoring shear
Mode III

Figure 1: *Fracture Modes*.
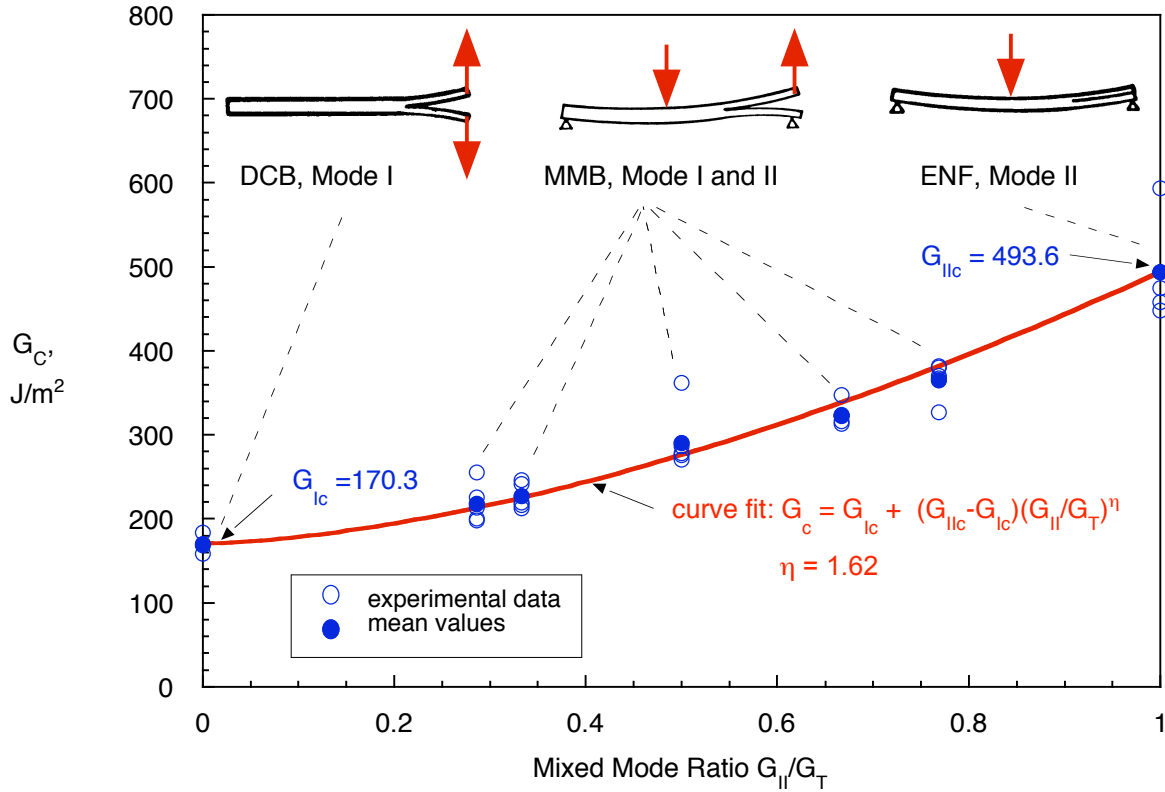
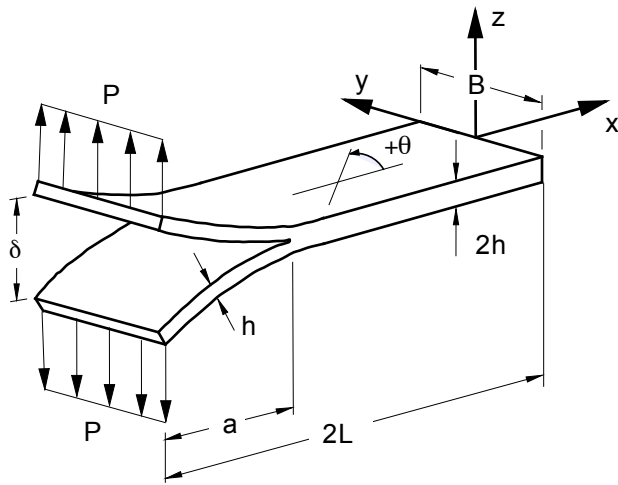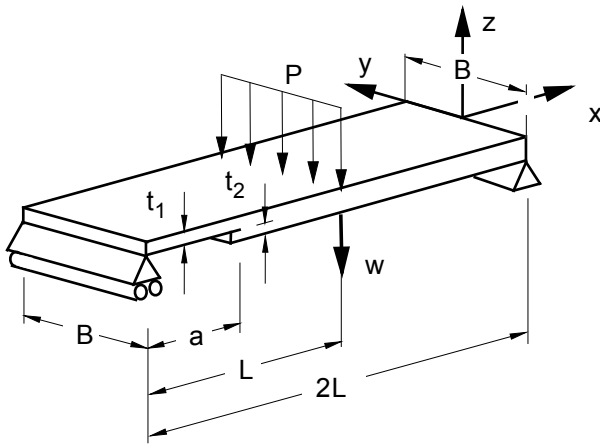Figure 2a. *Mixed-mode fracture criterion for T300/914C.*
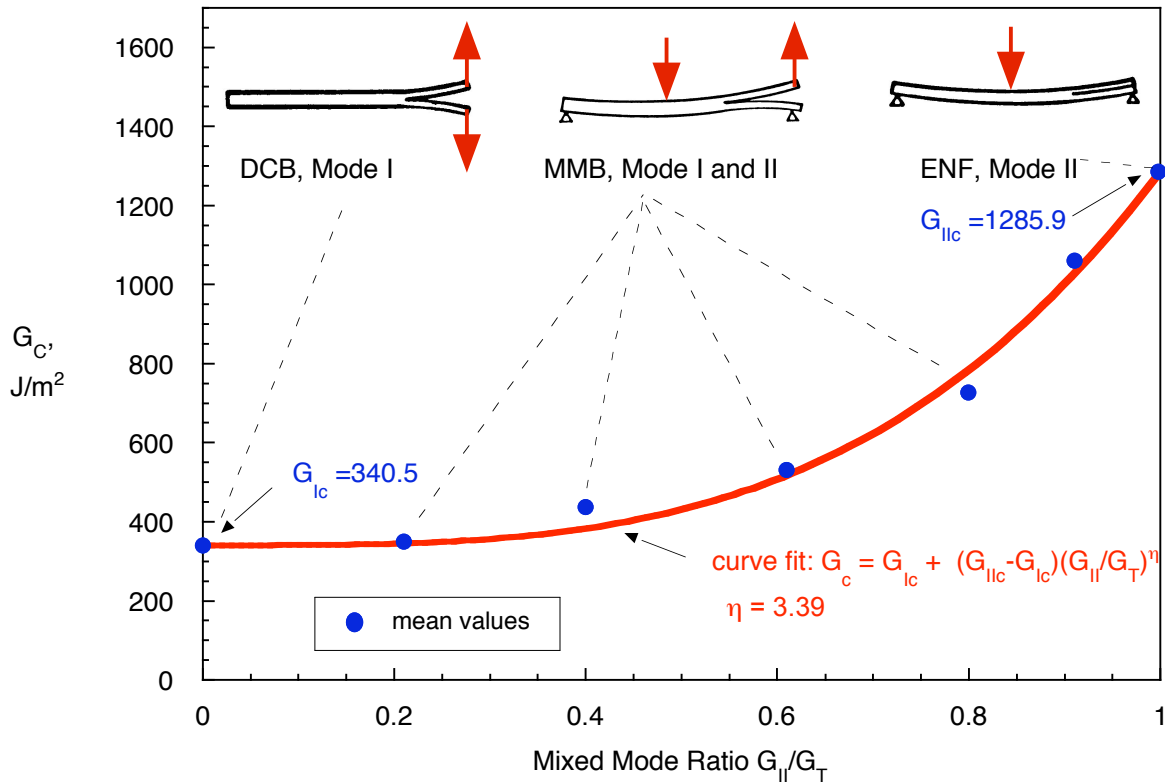
Figure 2b. *Mixed-mode fracture criterion for C12K/R6376.*

B	25.0 mm
2h	3.0 mm
2L	150.0 mm
a	30.0 mm

T300/914C $[0]_{24}$

(a) **D**ouble **C**antilever **B**eam Specimen (DCB)

B	25.4 mm
t_1	2.03 mm
t_2	2.03 mm
2L	177.8 mm
a	34.0 mm

D30: C12K/R6376 [±30/0/-30/0/30/0$_4$/30/0/-30/0/-30/30//-30/30/0/30/0/ -30/0$_4$/30/0/30/0/±30]

(b) **S**ingle **L**eg **B**ending Specimen (SLB)

Figure 3. *Specimen configurations.*

dimensions
B   25.0 mm
2L   150.0 mm
a   30.0 mm
2h   3.0 mm
i   2.0 mm

B

2L

bonded
nodes

top and bottom
surface

detail of local
model around
delamination front

i

2h

bonded
nodes

delamination front

top surface

bottom surface

z

y   x

a
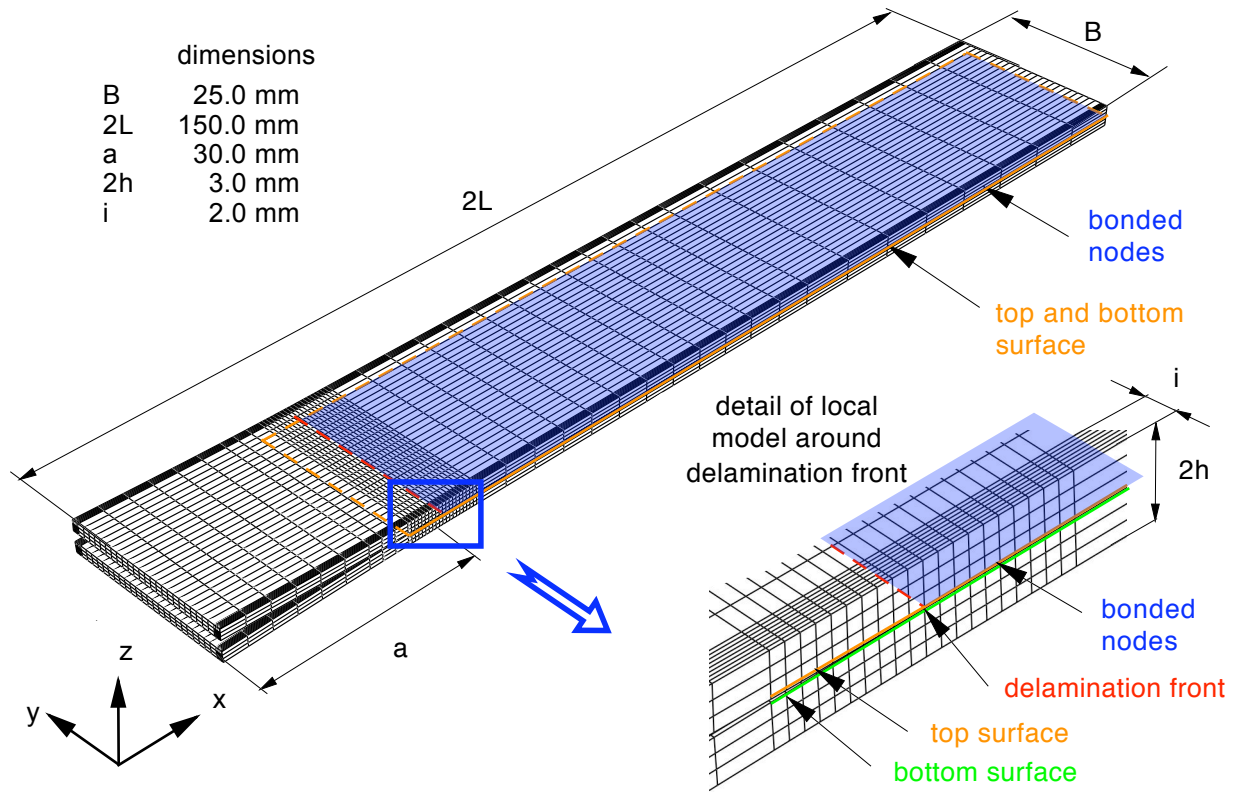
a. *Deformed model of DCB specimen with refined edges*

bonded nodes

initial straight delamination front

z

y   x
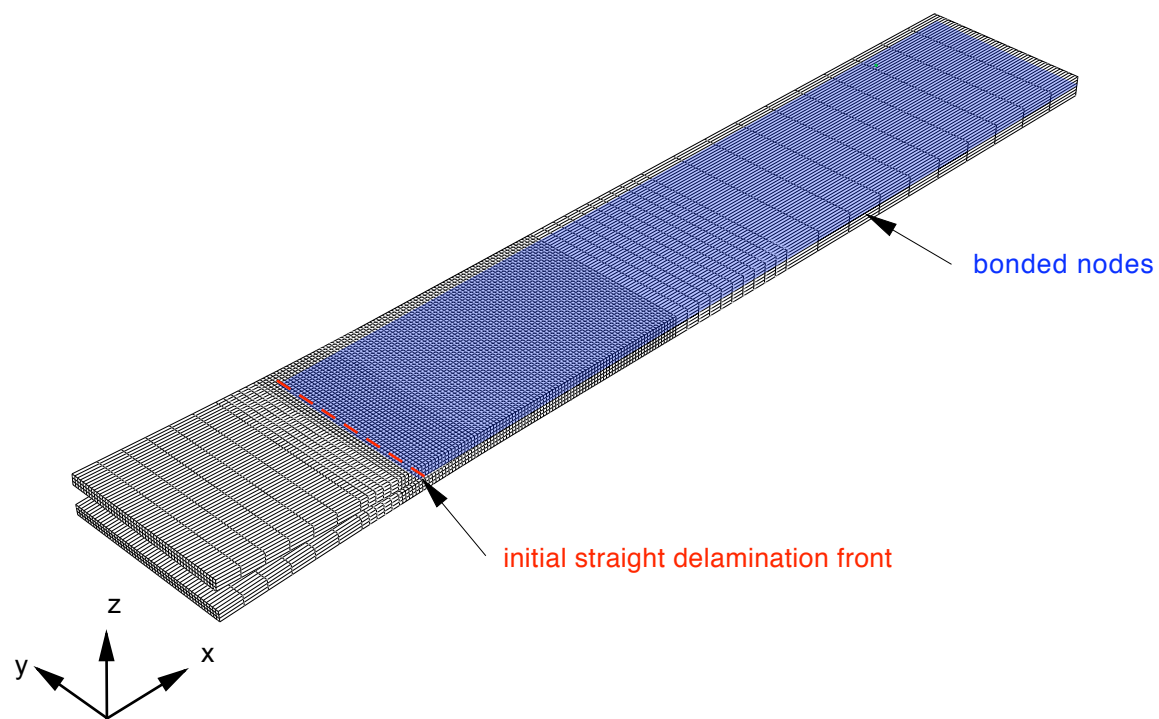
b. *Deformed model of a DCB specimen for VCCT for ABAQUS analysis*
Figure 4. *Full three-dimensional finite element model of a DCB specimen.*

dimensions

B   25.4 mm
2L   177.8 mm
M   180.0 mm
t_1 2.0 mm
t_2 2.0 mm
a   34.0 mm

B

M
2L

bonded
nodes

top and bottom
surface

initial straight delamination front

z

y   x

a

support of upper arm
across the width of
the specimen

detail of local
model around
delamination front

t_1

t_2

bonded
nodes

delamination front

top surface

bottom surface

[30/0/30/0/±30]

[0]$_4$

[0/30/0/ -30]

[30]

[-30]

[30]

[-30]

[30/0/-30/0]

[±30/0/-30/0/30]

[0]$_4$

D30: [±30/0/-30/0/30/0$_4$/30/0/-30/0/-30/30/-30/30/0/30/0/ -30/0$_4$/30/0/30/0/±30]

Figure 5. *Deformed model of SLB specimen and detail of region around delamination front.*
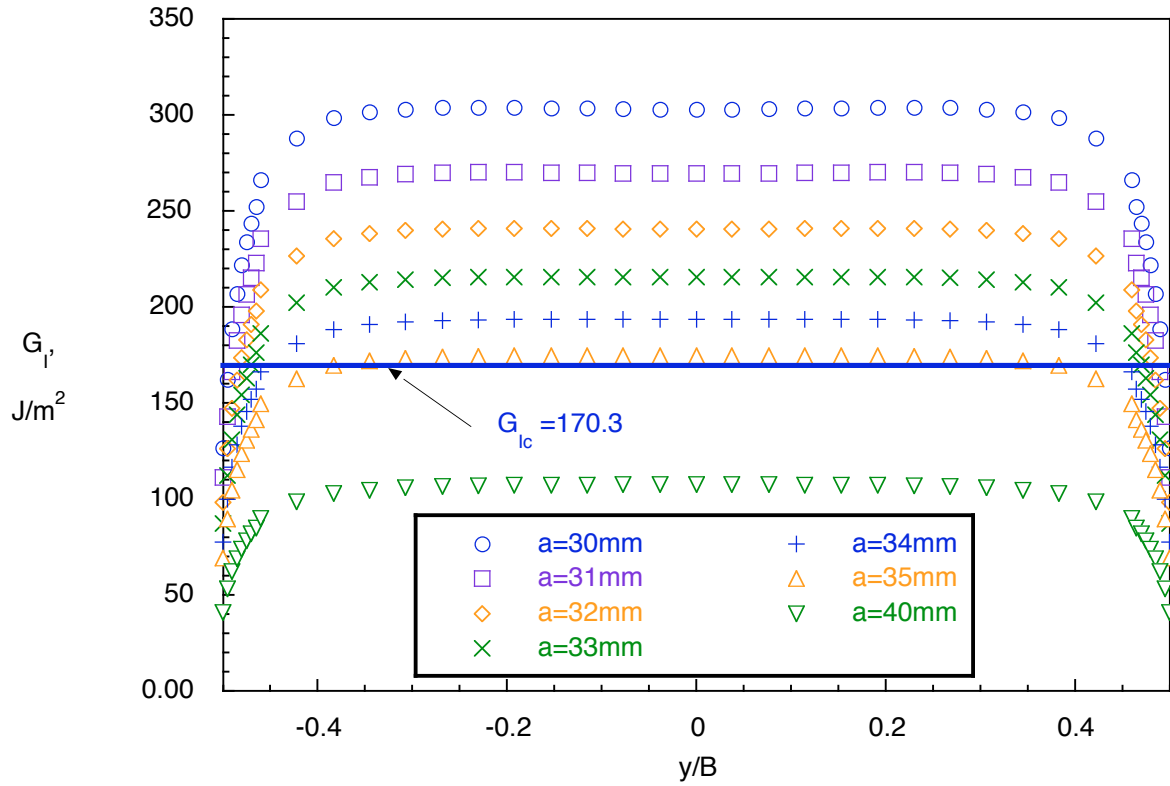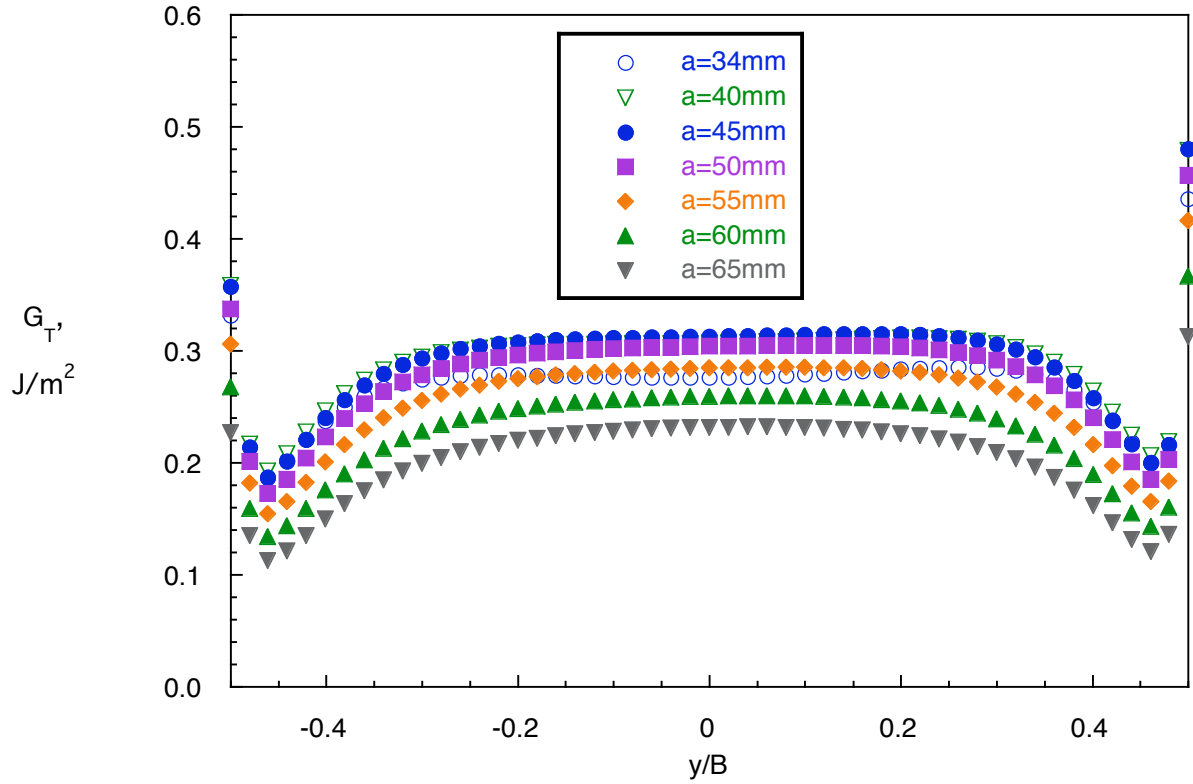
Figure 6a. *Computed strain energy release rate distribution across the width of a DCB specimen (model Figure 4a).*
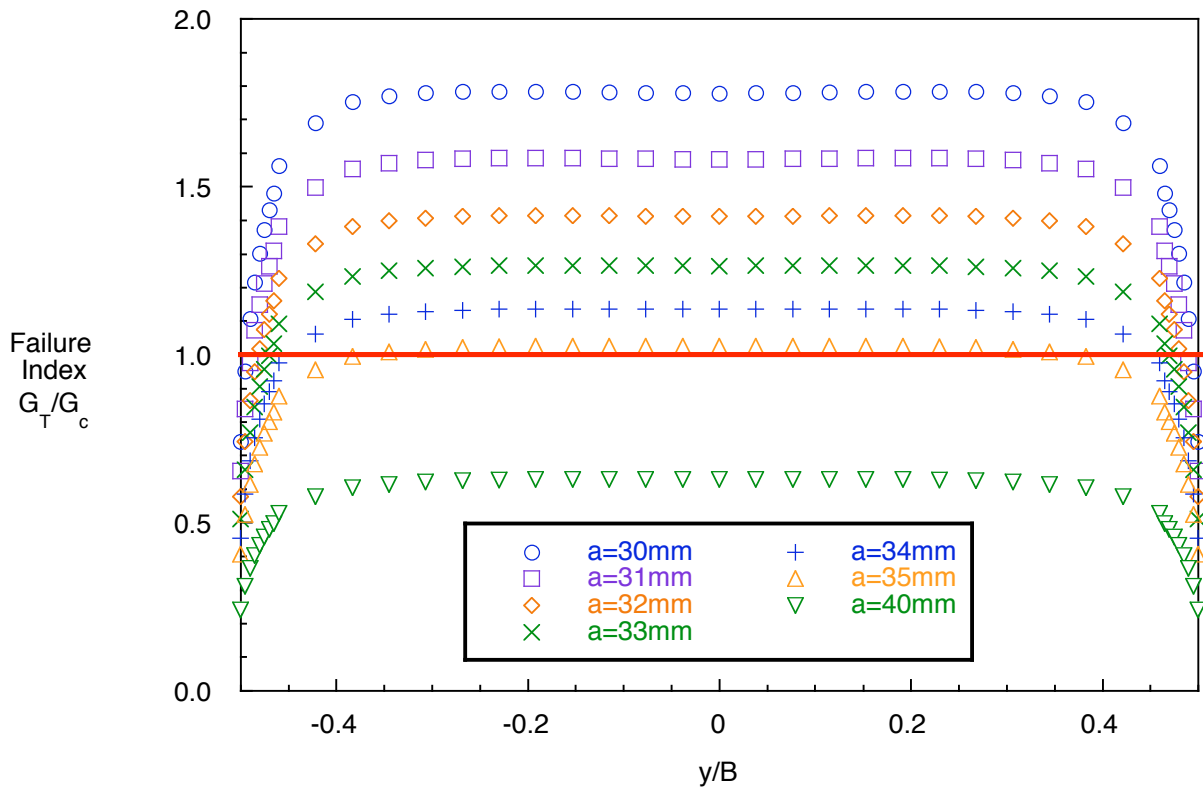
Figure 6b. *Failure index distribution across the width of a DCB specimen(model Figure 4a).*
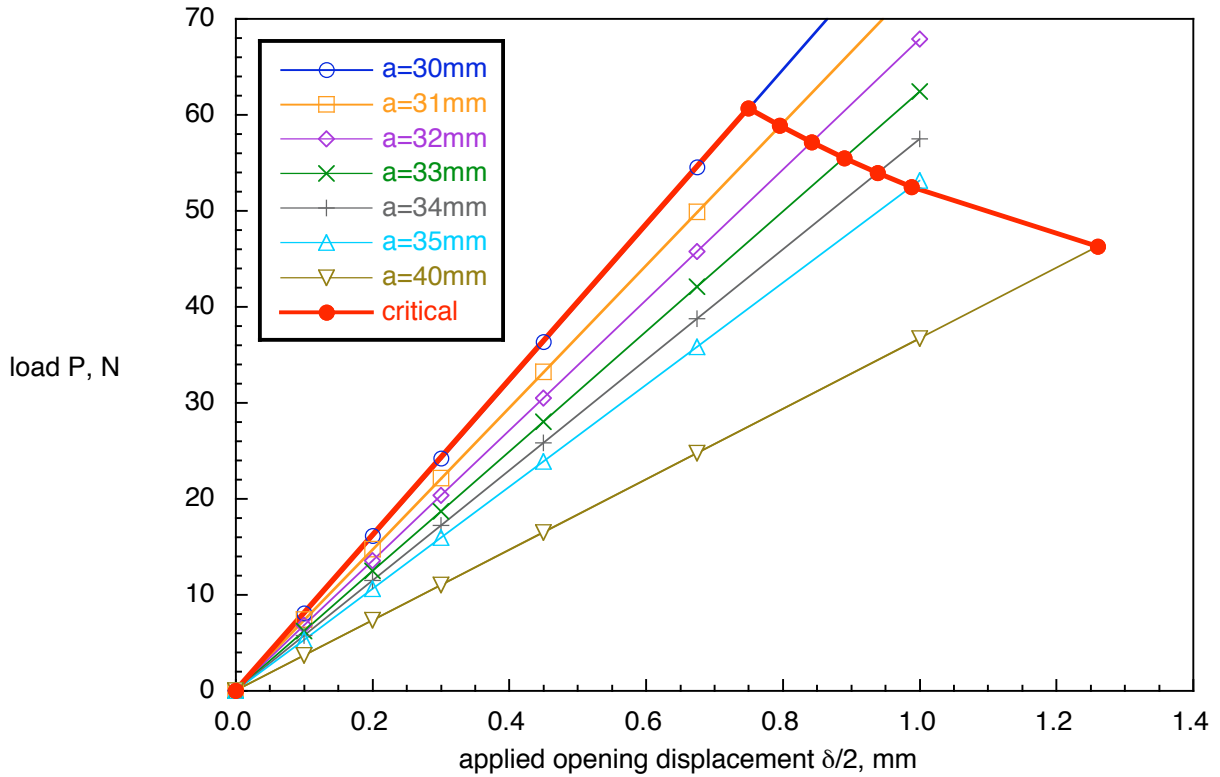
Figure 7a. *Benchmark: Critical load-displacement behavior for DCB specimen.*
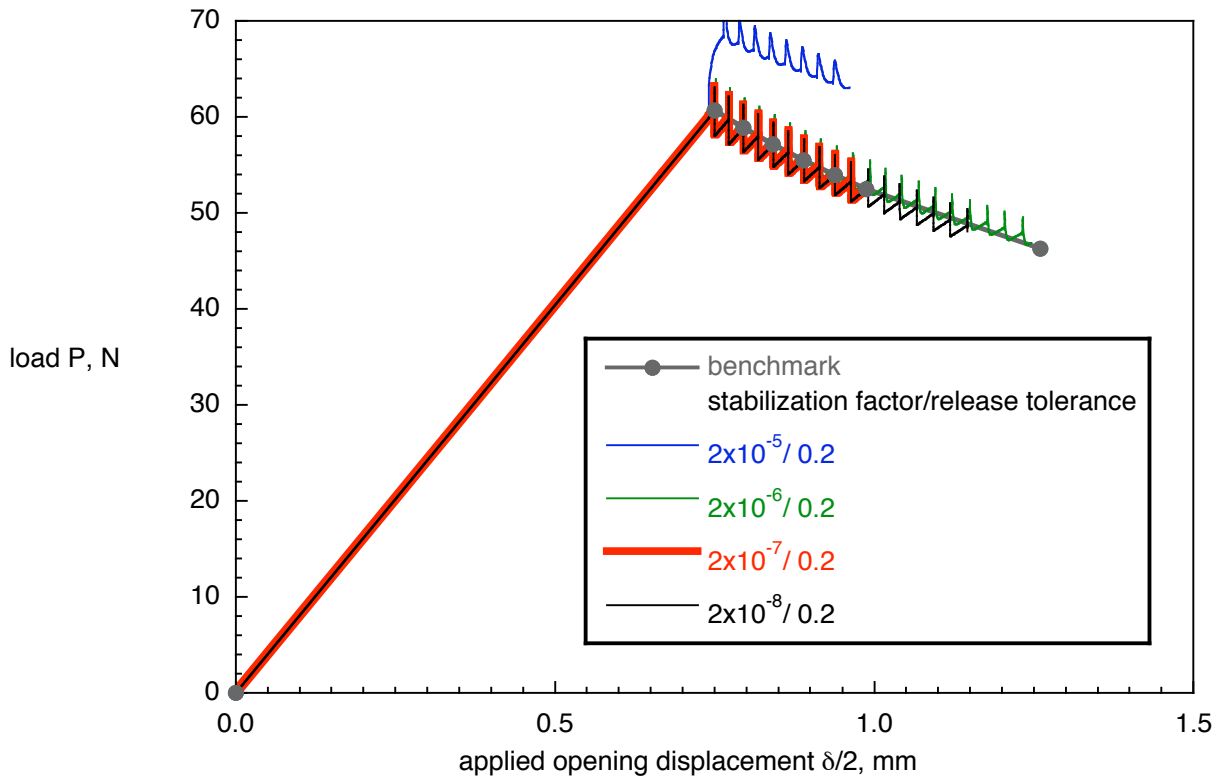
Figure 7b. *VCCT for ABAQUS: Computed critical load-displacement behavior for DCB specimen obtained from results with global stabilization.*
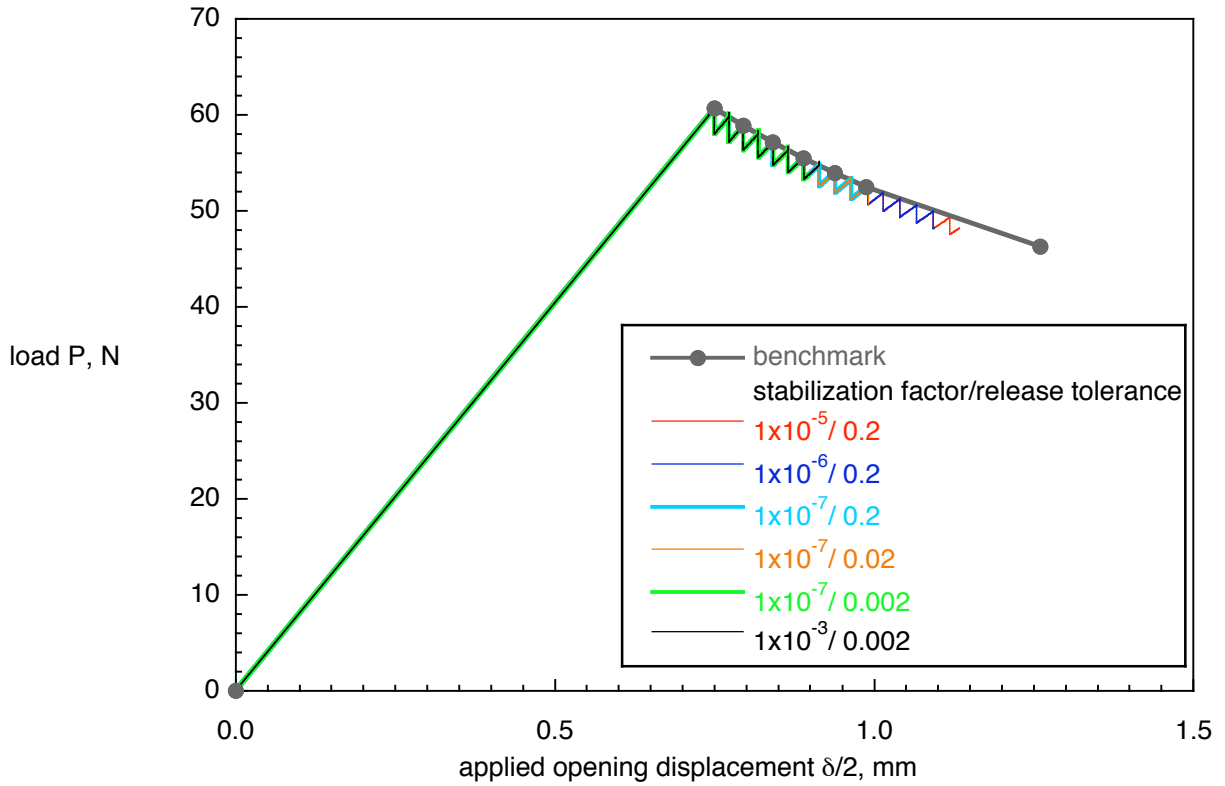
Figure 8a. *Computed critical load-displacement behavior for DCB specimen obtained from results with contact stabilization.*
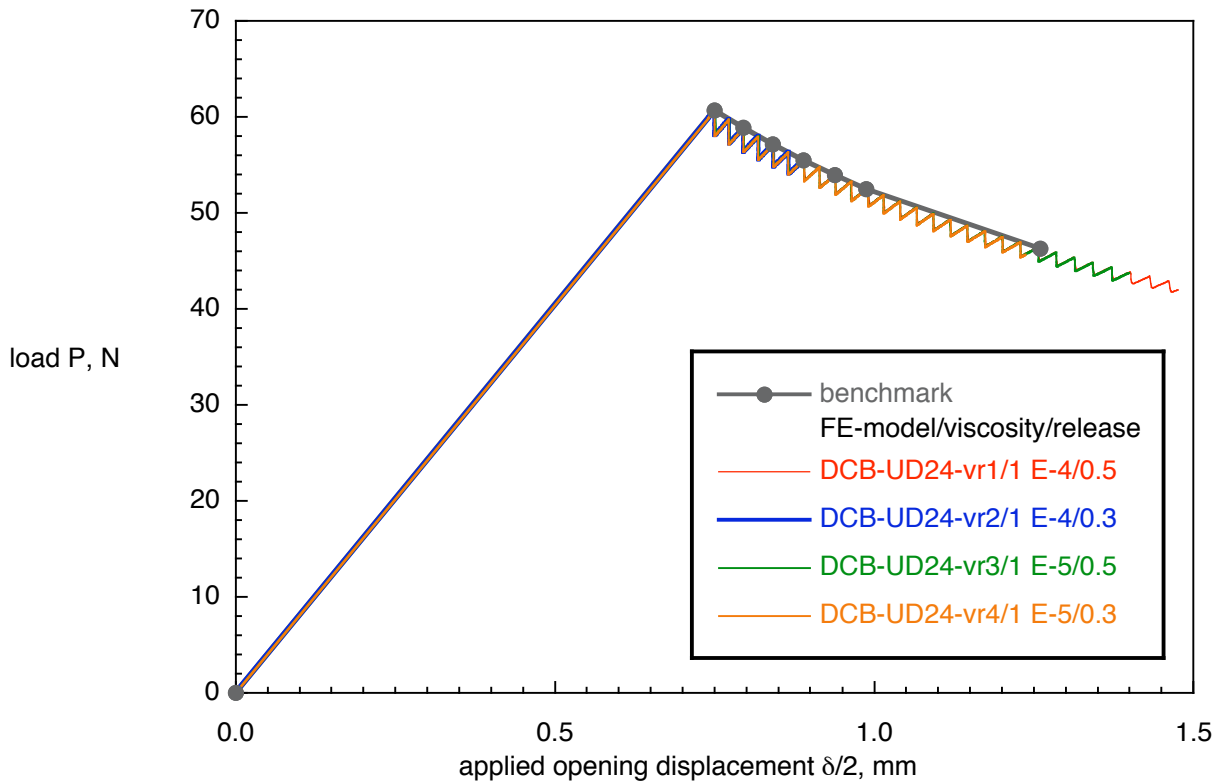
Figure 8b. *Computed critical load-displacement behavior for DCB specimen obtained from results with viscous regularization.*
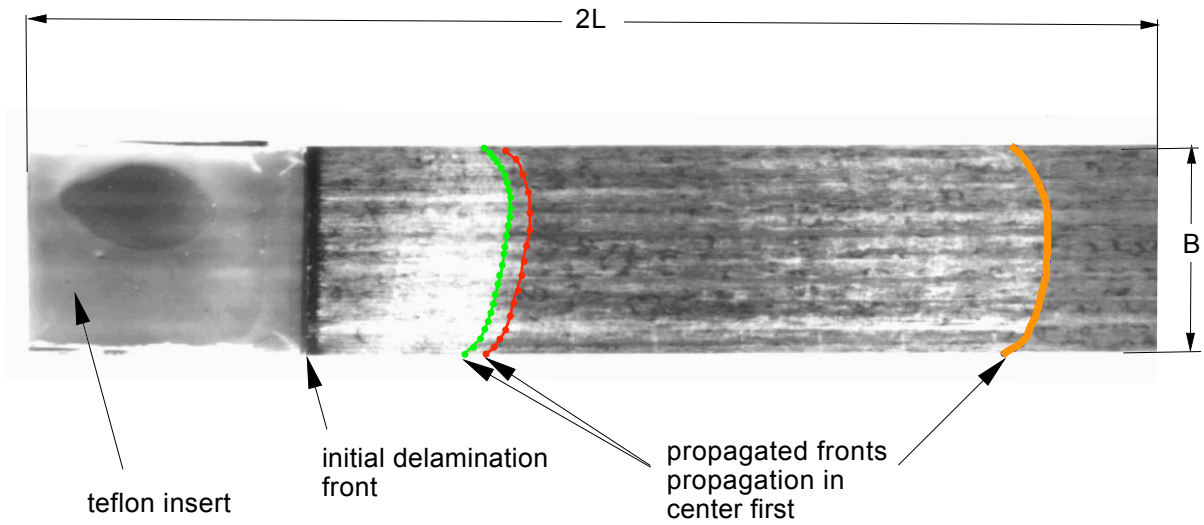
(a) Scan of fractured DCB specimen
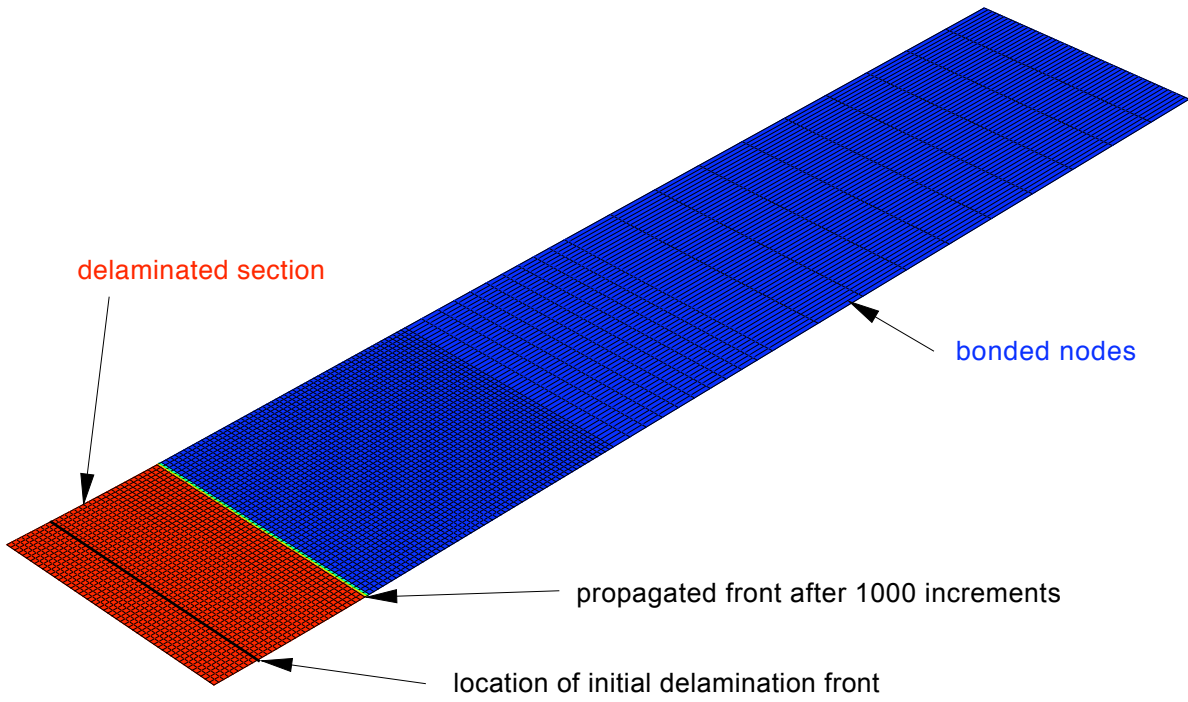
(b) Delamination front after 1000 increments (Bottom surface of FE model in Figure 4b)

Figure 9. *Delamination front shape for a DCB specimen.*

Figure 10a. *Computed strain energy release rate distribution across the width of a SLB specimen.*
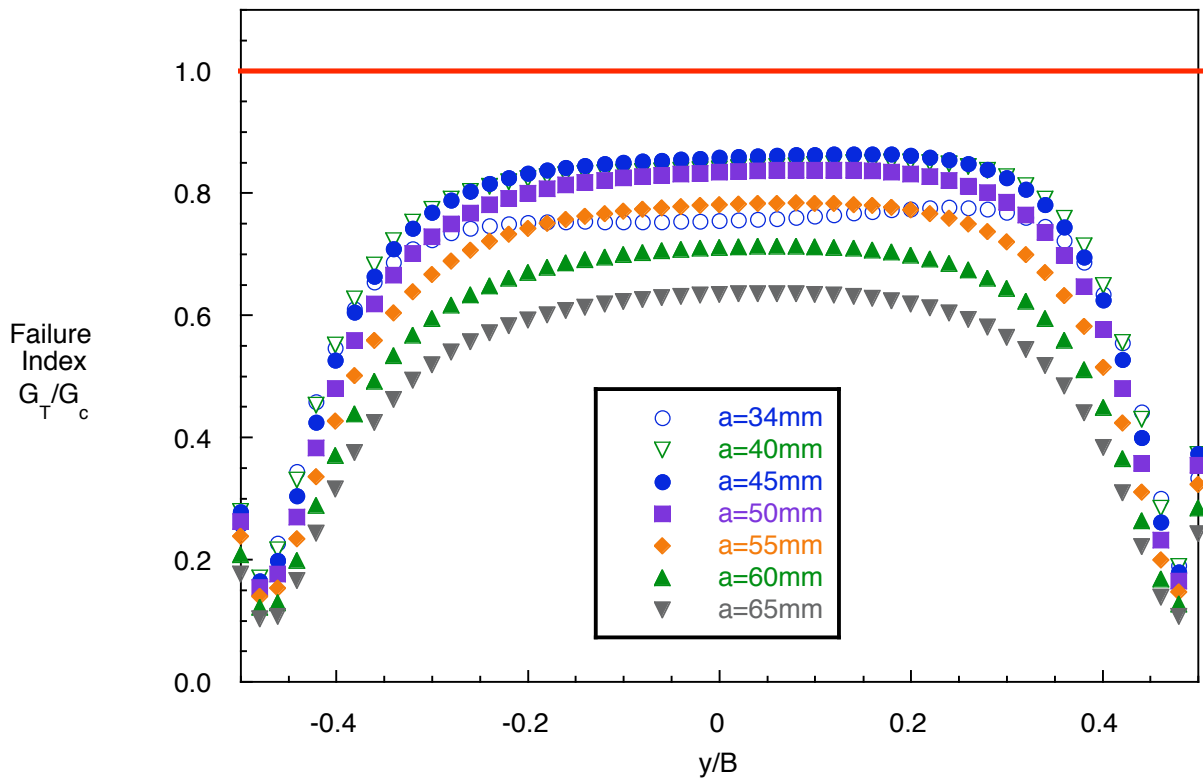
Figure 10b. *Failure index distribution across the width of a SLB specimen.*
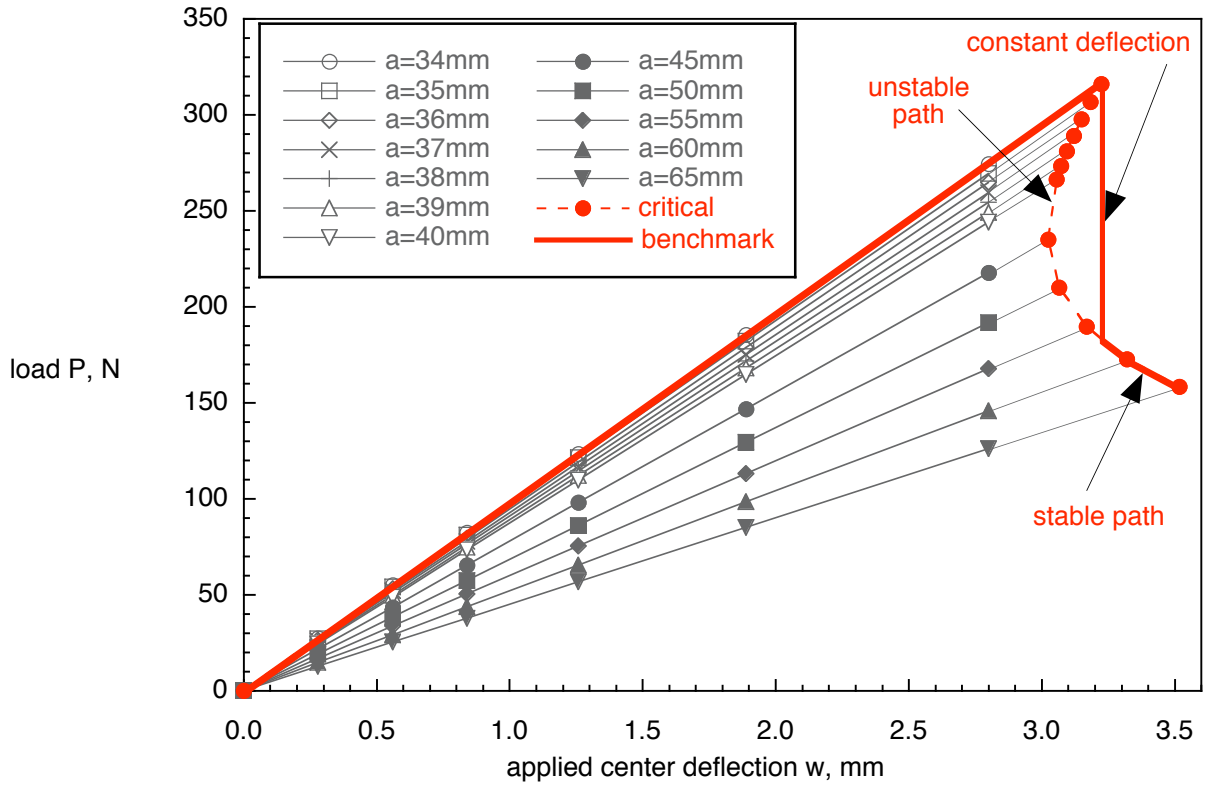
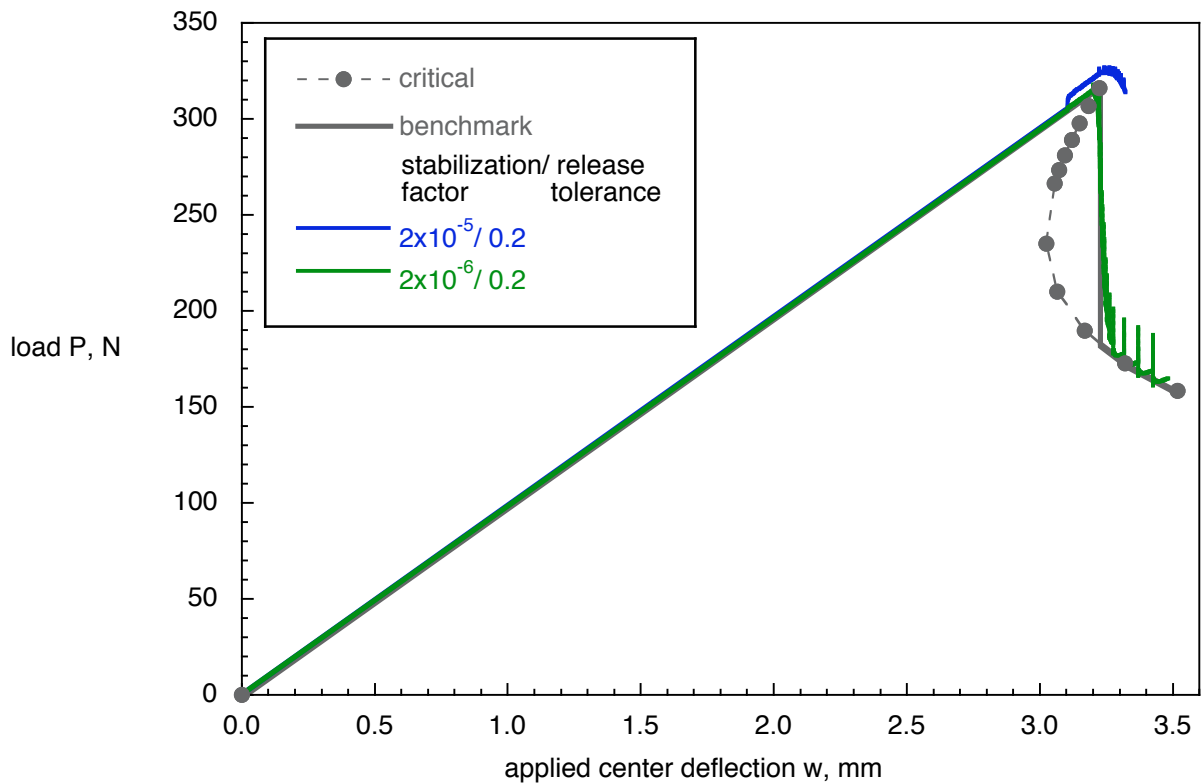Figure 11a. *Critical load-displacement behavior for SLB specimen.*

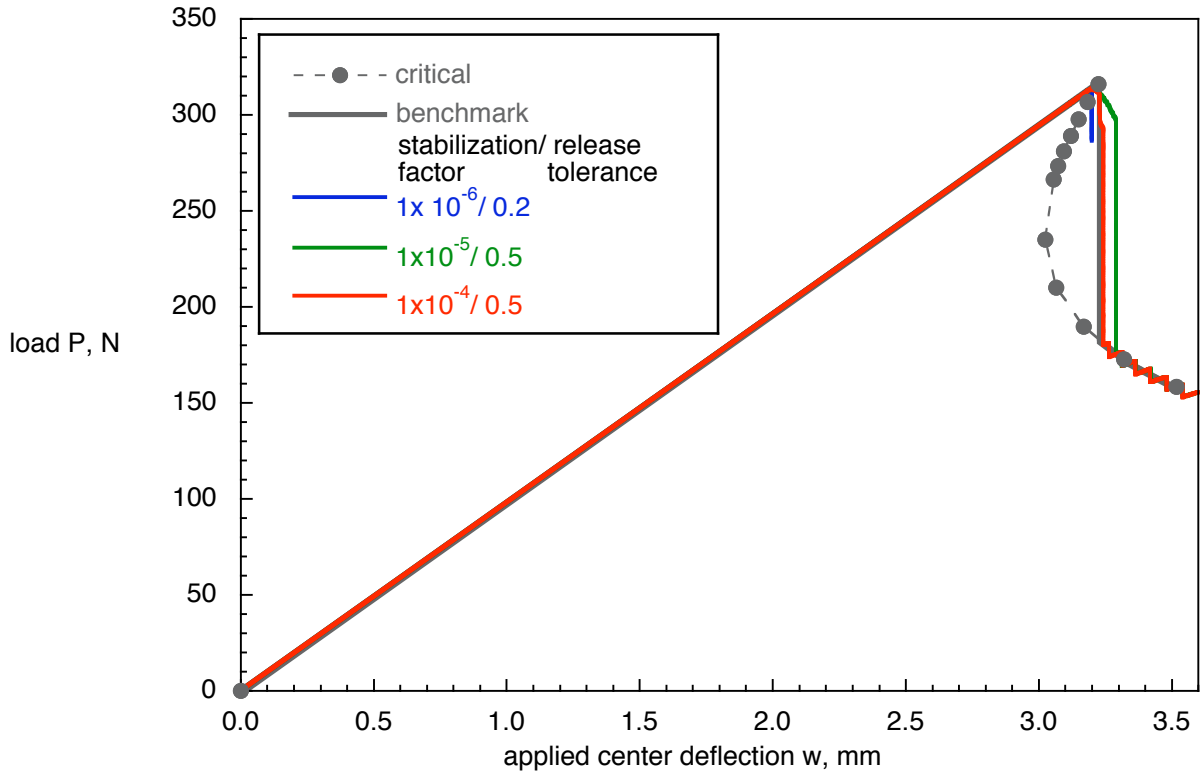Figure 11b. *Computed critical load-displacement behavior for SLB specimen obtained from results with global stabilization.*

Figure 12a. *Computed critical load-displacement behavior for SLB specimen obtained from results with contact stabilization.*
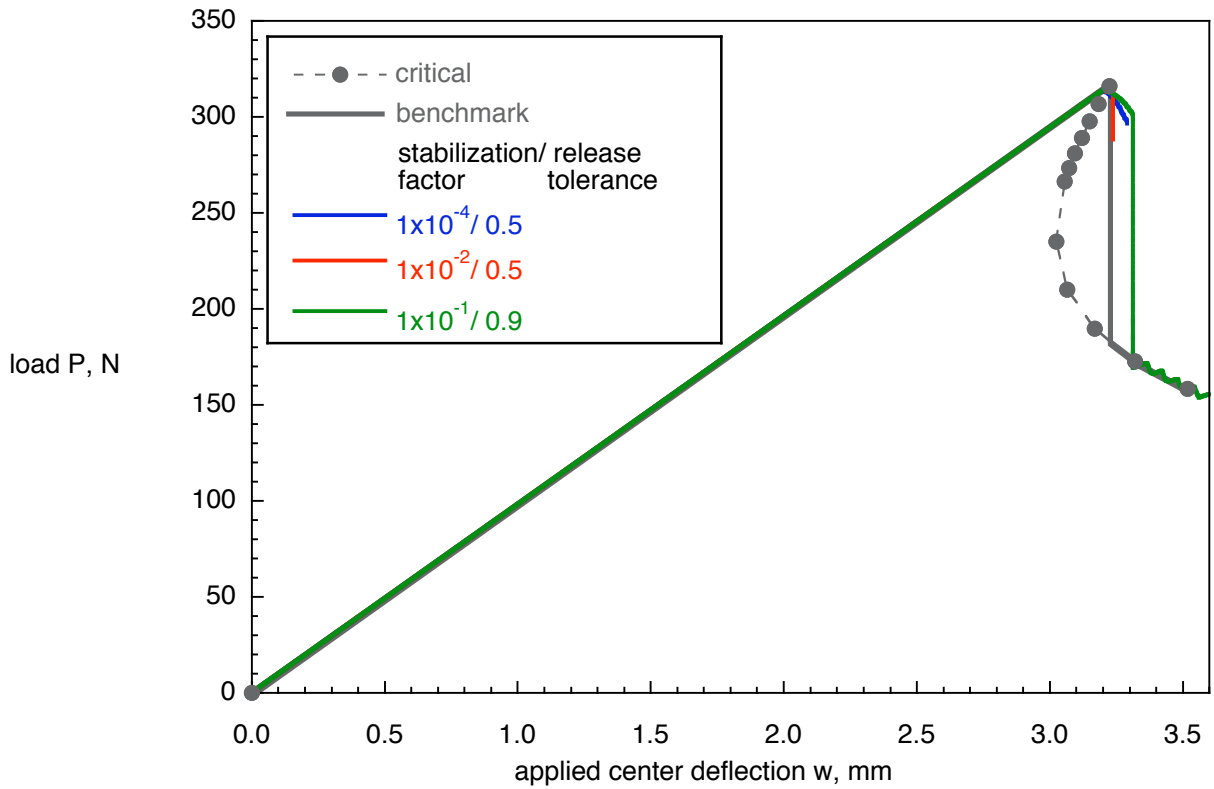

Figure 12b. *Computed critical load-displacement behavior for SLB specimen obtained from results with viscous regularization.*
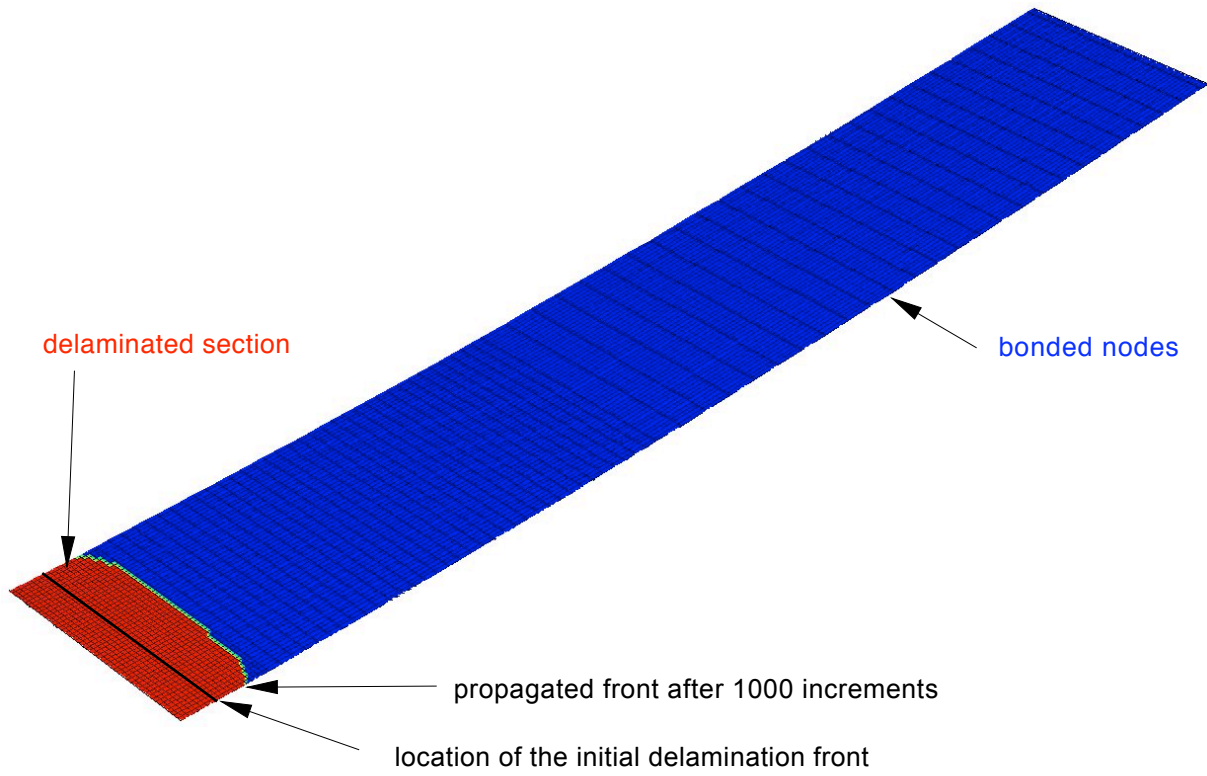
Figure 13. *Delamination front for a SLB specimen (Bottom surface of FE model in Figure 5).*